American Mineralogist, Volume 93, pages 1799–1815, 2008

Nano to macroscale biomineral architecture of red coral (*Corallium rubrum*)

Daniel Vielzeuf,[1,*] Joaquim Garrabou,[2] Alain Baronnet,[1] Olivier Grauby,[1] and Christian Marschal[2]

[1]Centre Interdisciplinaire de Nanosciences de Marseille, CNRS and Aix-Marseille Université, Campus de Luminy, 13288 Marseille, France
[2]Centre d'Océanologie de Marseille, UMR-CNRS 6540 DIMAR, Station Marine d'Endoume, rue Batterie des Lions, 13007 Marseille, France

Abstract

Different techniques have been used to characterize the physical and chemical structure of the red coral calcitic skeleton. A section normal to the axis of the skeleton shows a medullar zone surrounded by a circular domain composed of concentric rings. Growth rings are revealed by the cyclic variation of organic matter (OM) and Mg/Ca ratio. These growth rings are annual; thus, both OM and Mg/Ca ratio can be used to date red coral colonies. Growth rings display wavelets. The internal structure of each wavelet results from the stacking of layers with tortuous interfaces. Tortuosity is due to the presence of microprotuberances. Interfaces between layers may display sharp discontinuities indicative of interruption of the mineralizing process. SEM and TEM studies show that each layer is made of (1) fibers, organized or not in fan-shaped structures; and (2) submicrometer (apparently mono-) crystalline units. Fibers are superstructures made of submicrometer units possibly assembled by an oriented aggregation mechanism. HRTEM studies show that in spite of displaying single-crystal scattering behavior, the submicrometer crystalline units are made of 2–5 nm nanograins again possibly aggregated by a mechanism of oriented attachment. Thus, submicrometer crystalline units and polycrystalline fibers can be both defined as mesocrystals. The red coral skeleton is a hierarchically organized organic-inorganic composite that exhibits porosity and structural and compositional order on length scales from the nanoscale to the macroscale.

Keywords: Red coral, growth ring, biomineralization, three-dimensional micro-nano hierarchical structure, mesocrystal, nanograin, calcite

Introduction

Marine biological organisms produce skeletons or shells that are composite materials made of minerals and organic components (Meldrum 2003). A major interest of biomineral structures is that their chemical composition and physical structure can vary under the influence of external conditions. Thus, "biorocks" have the ability to record environmental forcings and represent potential archives of past environmental conditions. However, deciphering the three-dimensional architecture of biomaterials and the mechanisms of their construction is difficult because of the complexity of their structure, the requirement of a wide spectrum of analytical techniques, and the integration of spatial observations covering several orders of magnitude. As a consequence, few biomineral structures are fully understood.

Red coral, *Corallium rubrum* (Linnaeus 1758) (Cnidaria; Anthozoa; Octocorallia), is an emblematic species of the Mediterranean Sea. It is mainly distributed in the western Mediterranean basin at depths ranging from 10 to 200 m. Red coral is a long-lived colonial and sessile organism (Barletta et al. 1968; Liverino 1989). The main morphological features of the red coral have been described in the pioneering work of Lacaze-Duthiers (1864). Red coral is composed of a solid red, mostly inorganic, axial skeleton (Fig. 1a) coated with living tissues (coenenchyme). A cellular layer (ectoderm) forms the external surface of the coenenchyme. Under the ectoderm, the mesoglea is composed of a thick acellular gelatinous layer of collagen (Grillo et al. 1993). Inside the mesoglea, small canals form a complex network communicating with (1) large gastrodermal canals running parallel to the axial skeleton, and (2) polyps. The mesoglea contains small (~30–50 μm) calcareous granules (sclerites is synonymous to spicules) that give a granular appearance to the living tissues (Grillo et al. 1993). Both kinds of skeletal structures (axial skeleton and sclerites) are made of Mg-rich calcite. Allemand et al. (1994) demonstrated the presence of an organic component representing 1.2 and 1.7 wt% in the axial skeleton and the sclerites, respectively.

In spite of detailed studies (Mateu et al. 1986; Allemand and Grillo 1992; Allemand 1993; Grillo et al. 1993; Allemand et al. 1994; Weinbauer et al. 2000; Marschal et al. 2004), the internal structure of the axial skeleton of the red coral is not understood. In particular, the spatial relations between the physical structure

* E-mail: vielzeuf@cinam.univ-mrs.fr

and the chemistry remain in great part unexplored. The goal of this study was to carry out a multiscale physico-chemical characterization of the mineral part of the red coral skeleton for a better understanding of its three-dimensional architecture.

Materials and methods

Biological material

Most of the red coral colonies in this study come from the rocky coast near Marseille (France) and the Medes islands (Spain). A few other colonies from Corsica (France) and Cap de Creus (Spain) were also studied. At these localities, the common ocurrence of submerged caves and overhangs together with strong local currents, wind-induced water movements, and the nearness of rivers favor the development of red coral at shallow depths (Laborel and Vacelet 1961; Ros et al. 1984; Marschal et al. 2004). Surfaces of the axial skeleton of different colonies were observed with an optical microscope and a scanning electron microscope (SEM) in secondary electron (SE) mode after removal of the organic tissues by immersion in diluted H_2O_2. Broken sections of the axial skeleton, with or without H_2O_2 treatment, were also observed with an SEM by SE imaging. Other axial skeleton sections were mounted in epoxy and polished for electron microprobe (EMP) X-ray mapping and chemical analyses, and/or SEM observations by back-scattered electron (BSE) imaging. After elemental mapping by EMP or SEM, some of the polished sections were etched in H_2O_2 to reveal their fine-scale surface structure. A polished section of the axial skeleton parallel to its axis and still surrounded by the dried organic tissues containing sclerites was also prepared for complementary observations and preparation of focused ion beam (FIB) foils. A technique of organic matter (OM) staining developed by Marschal et al. (2004) was also used to characterize the OM distribution. One of the difficulties of our integrated approach resided in applying various techniques with significantly different spatial resolutions (from a few millimeters down to a few nanometers) to the very same, well-localized sample surface. Because of the irreversibility of some sample treatments, care had to be taken to define a protocol of observations from less to most destructive.

Techniques

Scanning electron microscope (secondary electron mode). Surface images of coral skeletons were obtained using field-emission scanning electron microscopes in secondary electron (SE) mode (JEOL 6320F at CINaM, Marseille; LEO 1550VP at Caltech, Pasadena). Samples were carbon-coated and operating conditions were 3 to 15 kV accelerating voltage with a working distance of 6 to 15 mm at Marseille, and 10 kV accelerating voltage with a 3 mm working distance at Caltech.

SEM (back-scattered electron mode). Compositional contrast imaging was carried out using a conventional tungsten filament SEM JEOL 5910LV at LMV, Clermont-Ferrand. This SEM is equipped with a Princeton Gamma-Tech X-ray analyzer operating in energy dispersive mode. The back-scattered electron mode was used on polished sections or blocks embedded in epoxy, with 20 kV accelerating

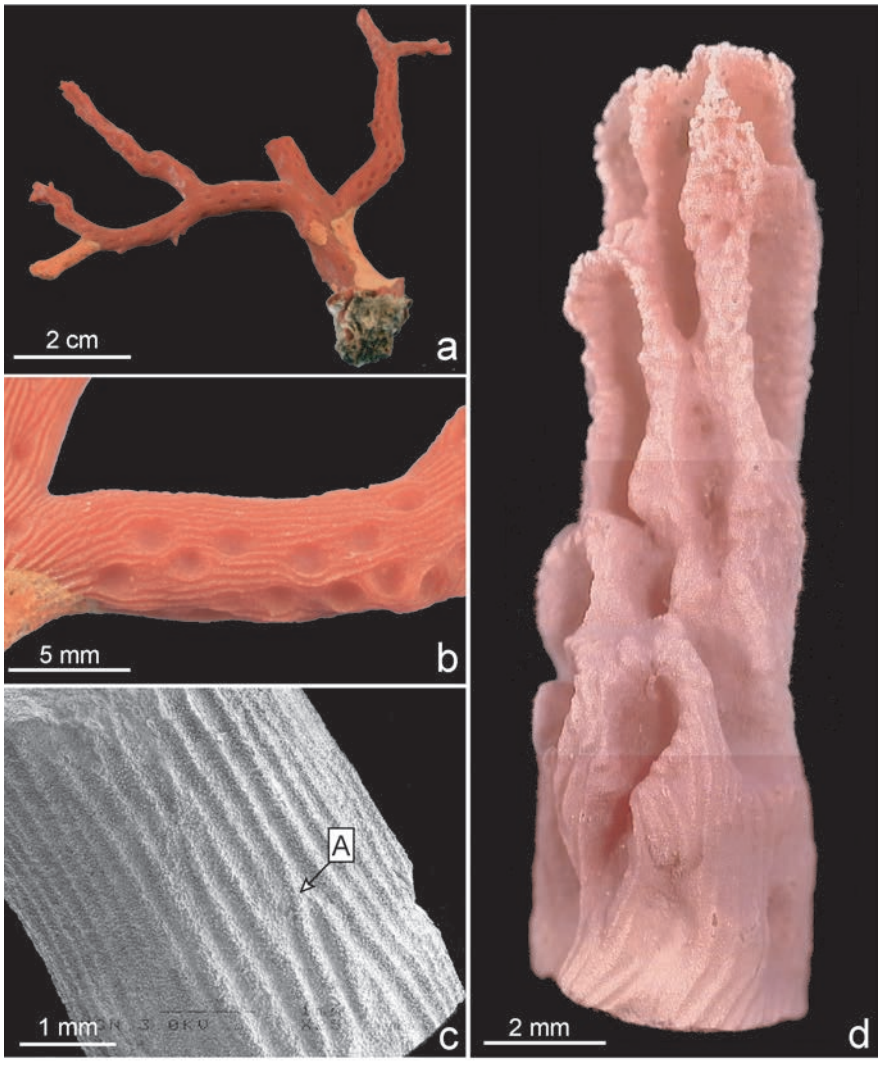

Figure 1. Macroscopic images of the skeleton of *Corallium rubrum*. (**a**) General view of a colony after partial removal of the living tissues (remnants of dried tissues appear orange). (**b**) Enlargement of **a** showing crenulations and polyp sites. (**c**) View of a characteristic subapical part of a branch with crenulations and bifurcations. (**d**) Apical part of a branch of red coral.

voltage, 2 nA probe current, and 19 mm working distance. Some BSE images were also obtained on a JEOL superprobe at ETH-Zurich. The efficiency of production of back-scattered electrons under the electron beam is proportional to the mean atomic number (Z) of the excited volume of the sample and results in image contrast as a function of composition: high average atomic number materials appear brighter than low atomic number ones. Holes appear in black and thus a material with high porosity will appear darker than the same material with low porosity. In the red coral skeleton, variations in chemical composition are not large and it is difficult to obtain contrasted back-scattered images.

Electron microprobe X-ray images and chemical analyses (EMPA). Most X-ray images of Ca, Mg, and S were obtained on a Cameca SX100 electron microprobe (LMV, Clermont-Ferrand). The definition of the X-ray images is usually 512 × 512 pixels. Three images were acquired at the same time during sessions that lasted ~8 h. At ETH-Zurich, the electron probe microanalyses (EPMA) and X-ray maps were performed on a JEOL JXA 8200 instrument equipped with five wavelength-dispersive X-ray spectrometers (WDS) and an energy dispersive spectrometer (EDS). All samples were coated with a ~20 nm thick carbon layer. For elemental distribution maps, an accelerating voltage of 15 kV, a beam current of 30 nA, and a beam diameter <1 µm were applied. Quantitative results (spot analyses and analytical traverses) were also obtained with electron microprobes. However, due to space constraints, these results will not be discussed here.

Transmission electron microscope (TEM). Some TEM samples were prepared with an ion mill from dismountable petrographic thin sections. Single-hole TEM copper grids (2 × 1 mm slot) were glued on the sections for support, detached, and thinned to electron transparency using a GATAN PIPS ion mill. A 20 nm thick layer of amorphous carbon was evaporated onto the sample to provide electrical conductivity of the specimen surface in the TEM. Observations were made through thin wedges surrounding the hole made by ion milling. Thin foils of the sample were also prepared by focused ion beam (FIB) on an FEI Model 200 TEM FIB at CP2M (Marseille). Details on the preparation of such foils are given elsewhere (Vielzeuf et al. 2007). The coral skeleton proved resistant, and 100 to 200 nm thick foils could be prepared without difficulty. Ion mill and FIB preparations are complementary: FIB foils can be cut normal to the sample surface and positioned with great precision. The counterpart is that the sample is relatively thick and contaminated by Ga, which limits high-resolution TEM imaging capabilities. Conversely, the ion mill preparation does not allow a precise location but the material is less contaminated, the sample is thinner at wedges, which makes high-resolution observations possible.

Two transmission electron microscopes at CINaM were used. A JEOL 2000FX TEM, operated at 200 kV (0.28 nm point-to-point resolution) was used for imaging the samples and for obtaining selected-area electron diffraction (SAED) patterns. A JEOL 3010 TEM, operated at 300 kV (0.21 nm point-to-point resolution) was used to record bright-field, high-resolution images of the samples. Low magnifications (300 000×) were used to minimize damage by the electron beam and to delay the transformation of calcite into lime.

Results

In this section, the main features of the red coral skeleton are presented from the macro- to the nanoscale. On the figures, features of interest are labeled A, B, etc. and indicated by arrows. In the text, such features are referred to by the figure number followed by the feature label; for example, feature B in Figure 1a is referred to as Figure 1a [B].

Macroscopically, red coral displays a typical arborescent structure (Fig. 1a), which can reach ~4 cm in basal diameter, 50 cm in height, and 3 kg in weight (Garrabou and Harmelin 2002). However, due to intense harvesting, colonies rarely exceed 1 cm in diameter and 10 cm in height in the NW Mediterranean region (Garrabou and Harmelin 2002). The tree-like structure of the red coral shows various fan- to bush-shape morphologies.

Medullar region

Stained preparations of perpendicular sections of the red coral axial skeleton (Figs. 2a–2e) allow a clear distinction between (1) a medullar region and (2) a surrounding domain made of concentric growth rings (annular region). In between, a transition zone displays intermediate characteristics. The medullar region is characterized by the absence of regular concentric rings and, most of the time, a ~2 mm bulbous-tip cross pattern (Figs. 2a, 2b, 2c, 2d [A]). Since a coral branch grows both in length and diameter, the medullar region must have been a branch tip at some stage of the growth of the organism. Thus, observation of a branch tip (Fig. 1d) provides information on the three-dimensional morphology of the medullar region. The first 5 to 10 mm part of the branch tip is thinner than the sub-apical part; it shows elongated pools with crenulated margins. The tip of the branch is granulated, porous, and friable whereas the sub-apical part is more massive and cylindrical (Figs. 1b and 1c). The pool shapes change progressively toward the base of the branch: they become rounded and shallower (Fig. 1d). The most prominent feature of the sub-apical region (Figs. 1a–1c) is the presence of characteristic longitudinal crenulations. Crenulations correspond to the position of gastrodermal canals as can be seen from the stained images (Fig. 2d [B]); they appear progressively within the first 5 to 10 mm from the tip of the branch (Fig. 1d). Interestingly, crenulations do not systematically surround the pools but interconnect them and are absent at the bottom (Grillo et al. 1993—their Fig. 1c, and our Fig. 1b). The rounded pools on the sub-apical part of the branch (Fig. 1b) correspond to previous emplacements of polyps (Grillo et al. 1993).

Annular region

Under the optical microscope, thin sections of the red coral skeleton show a conspicuous color banding (Fig. 2f). However, as shown by Marschal et al. (2004) and as can be seen from a comparison between Figures 2e and 2f, the staining of OM on polished sections reveals several growth rings within a single optical color banding. Each OM growth ring is made of two main bands: a dark thin band corresponding to a zone of high OM concentration and a wider light band where the OM concentration is low.

Different studies have shown that the calcite composing the axis skeleton of the red coral incorporates variable amounts of Mg (Milliman 1974; Maté et al. 1986; Weinbauer et al. 2000; Dauphin 2006). However, there is no information on the spatial distribution of this element within the skeleton. A series of Mg X-ray images were obtained on polished sections of different colonies. Figure 3a is an example of Mg mapping at relatively low spatial resolution: the darker gray zones correspond to low concentrations of Mg. This figure shows the highly ordered distribution of Mg and the presence of well-identified concentric and rippled growth rings. On the same polished section, the organic matter was stained and the results are shown in Figure 3c. The resemblance of the Mg and OM images is striking: both show the same ring features and the same periodicity. Figures 3b and 3d, which are enlargements of two coinciding zones in Figures 3a and 3c, respectively, display eight growth rings. For a comparison, the traces of the Mg-poor bands (dark bands in Fig. 3b) have been reported as white dashed lines on Figure 3d. This last figure indicates that the Mg-poor bands coincide with the richest OM zones. Plots of gray levels along a traverse (placement shown in Figs. 3a and 3c) obtained by image processing of the Mg and OM images confirm the anti-correlation between Mg and OM (Fig. 3g). In some cases, Mg-poor bands do not correspond to a par-

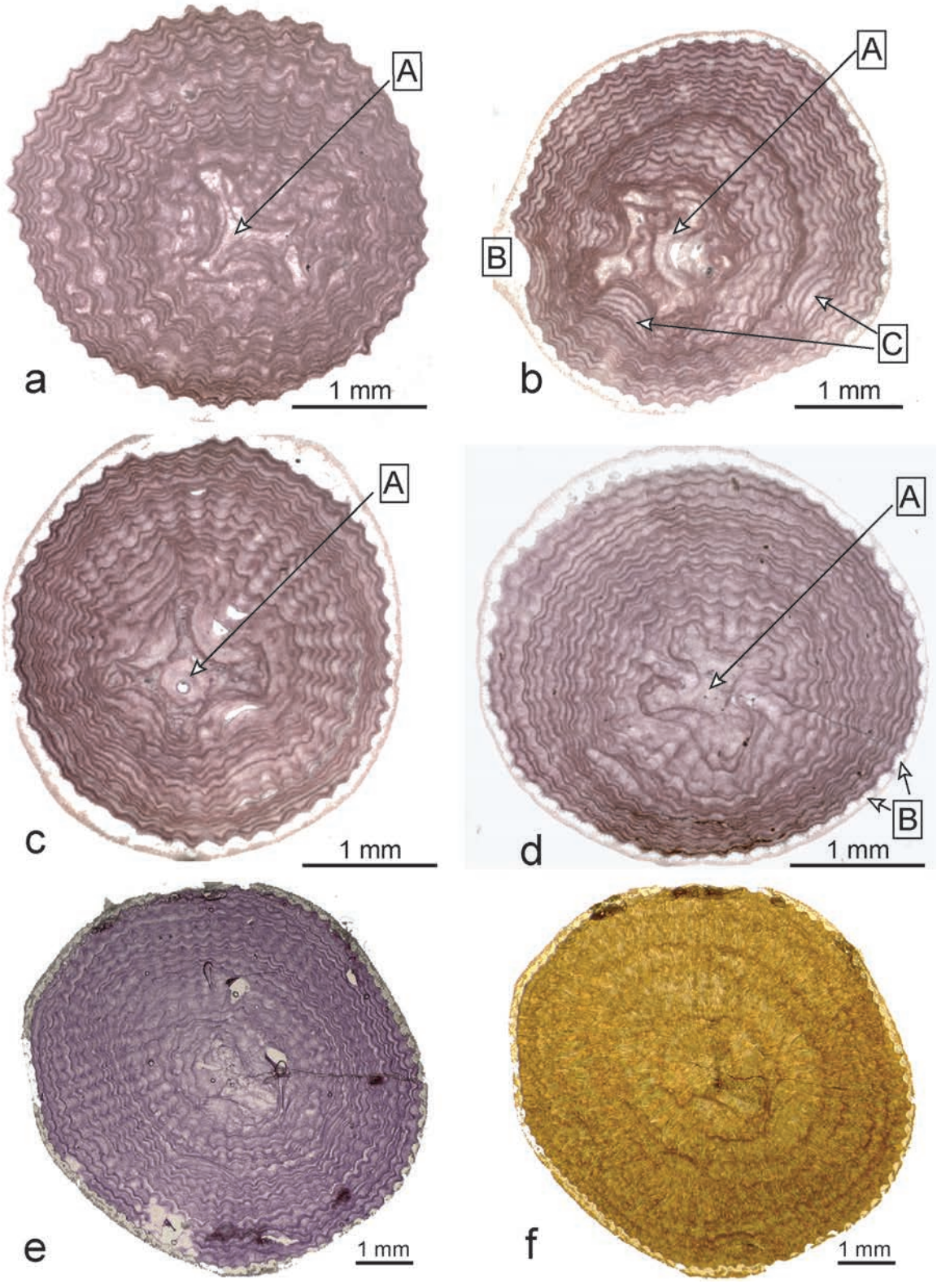

FIGURE 2. Sections of red coral skeleton after staining of the organic matter (OM). (**a–f**) Different examples of stained sections allowing the distinction between medullar and annular zones. (**f**) Thin section without OM staining under a petrographic microscope, same section as **e**. Note the difference in number and resolution of the growth rings between **e** and **f**.

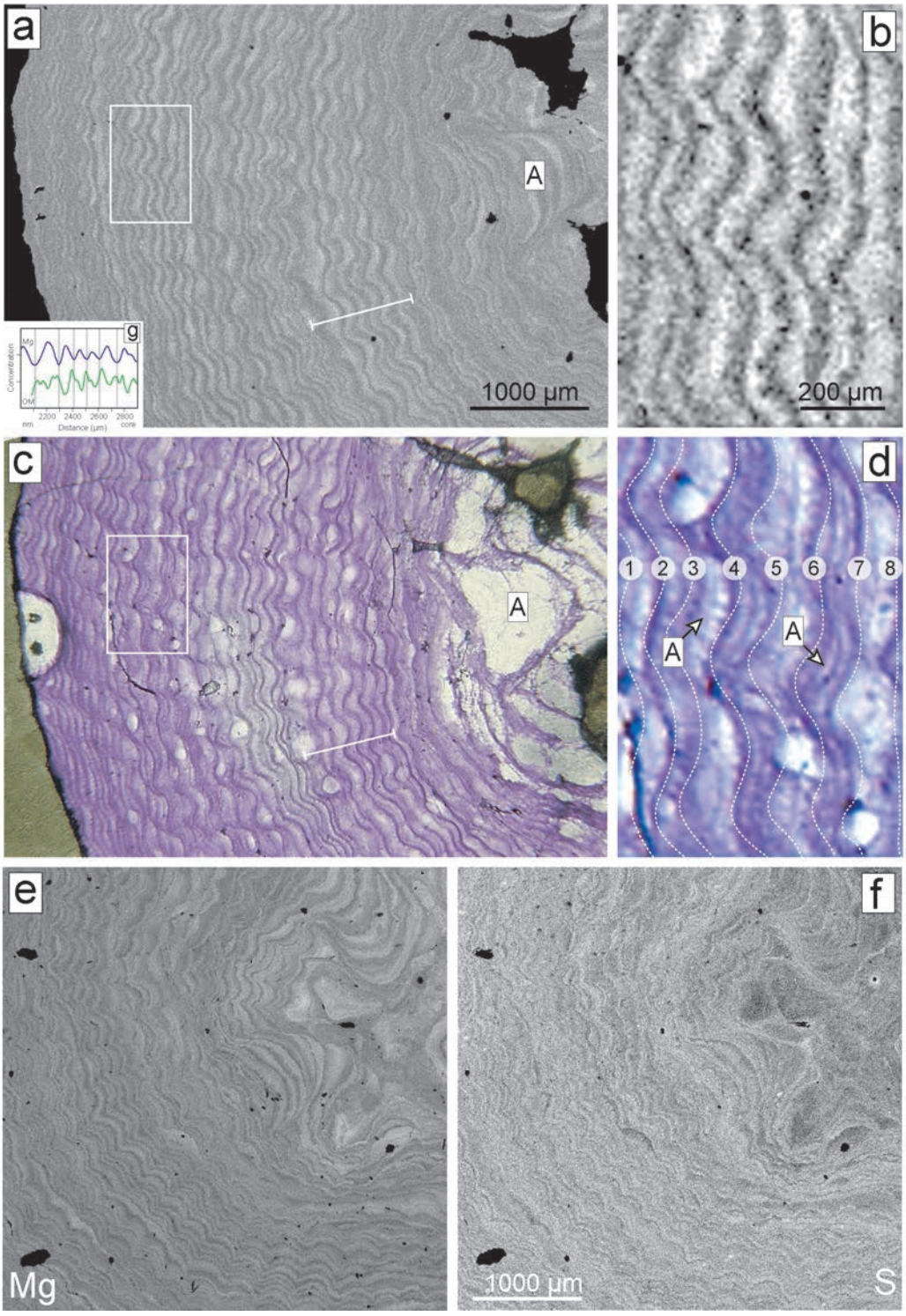

FIGURE 3. Distribution of Mg, OM, and S in two sections of red coral. (**a**) Distribution of Mg: dark zones are poor in Mg. The white rectangle indicates the location of the enlarged zone displayed in **b**. The white line is the location of a cross-section showing the relative concentrations of Mg and OM (insert **g**). (**b**) Distribution of Mg in the rectangular area shown in **a**. (**c**) OM distribution in same area as **a**. Note the similar periodicity of growth rings in **a** and **c**. The white rectangle is the location of the enlarged zone displayed in **d**. The white line is the location of the cross-section shown in insert **g** in **a**. (**d**) Distribution of OM in the rectangular area shown in **c**. The dashed white lines are the traces of Mg-poor bands in **b** indicating that Mg and OM are anticorrelated. Numbers 1 to 8 correspond to the numbering of annual growth rings. (**e** and **f**) Magnesium and S electron microprobe X-ray images of another section of red coral skeleton.

ticularly well-marked OM ring (e.g., ring 5 in Fig. 3d). The fact that the OM ring could fade locally was mentioned by Marschal et al. (2004). For this reason, these latter authors identified each growth ring around the whole section, and not simply across a traverse. This way, ring 5 can be identified in Figure 3c outside the magnified zone. Locally, the coincidence of Mg-poor with OM-rich bands is not perfect. For instance, close to the medullar zone, growth rings are not observed on the stained section (Fig. 3c [A]) but they are identified on the Mg image (Fig. 3a [A]). Indeed, Marschal et al. (2004) noted the fact that the OM growth rings were not always observed in the central part of large colonies. In addition, secondary internal OM structures can be observed both radial and normal to the main rings (Fig. 3d [A]) without equivalent on the Mg image. This observation is confirmed by the traverse (Fig. 3g) where OM peaks are commonly dedoubled without exact anticorrelation with the Mg signal. Thus, OM and Mg mappings reveal slightly different features. However, part of these differences can be due to artifacts. The staining method consists in decalcifying the sample to enhance the OM, and OM bands can be slightly displaced during the process. In addition, the relative low resolution of the Mg image in Figure 3a can explain some of the discrepancies. In all cases, differences remain slight and the fact that Mg-poor bands coincide with OM-rich zones must prevail.

A second series of X-ray images on a different sample (Figs. 3e and 3f) shows that medullar zones revealed earlier by OM staining method (e.g., Fig. 2) can be observed also on the Mg image. Here again the medullar zone displays a characteristic bulbous-tip cross pattern without concentric growth rings. However, this region is not chemically homogeneous and Mg-rich "islands" are present. Around the medullar zone, Figure 3e confirms that Mg heterogeneities and their arrangement in concentric rings is a general pattern.

Sulfur has been mentioned as a minor element in the skeleton of the red coral (Mateu et al. 1986; Grillo et al. 1993; Dauphin and Cuif 1999). However, like in the case of Mg, variations in concentration and spatial distribution have not yet been explored. Figure 3f is an X-ray image of the distribution of S within a section of red coral skeleton (same sample as in Fig. 3e). Although the image is not as sharp as the Mg image due to the very low concentrations of S (0.8 ± 0.1 wt% SO_3), the same features are observed: a medullar zone with a characteristic pattern, surrounded by concentric growth rings. A close comparison of the two images (Figs. 3e and 3f) shows that Mg and S are more or less anti-correlated. Combination of these observations with data presented earlier indicates that OM and S are correlated to some extent.

Wavelet

Concentric rings are riddled and display a succession of wavelets corresponding to the crenulations described earlier. The increase in circumference of the skeleton toward the rim is accommodated by an increasing number of wavelets. In Figure 4, 19 wavelets are present (and labeled) in the center of the section, and 47 compose the youngest ring. Thus, the wavelength of the wavelets remains fairly constant (~300 µm) throughout the coral sections (see Fig. 2). To clarify the structure, the ridges joining the crests of successive wavelets have been drawn on

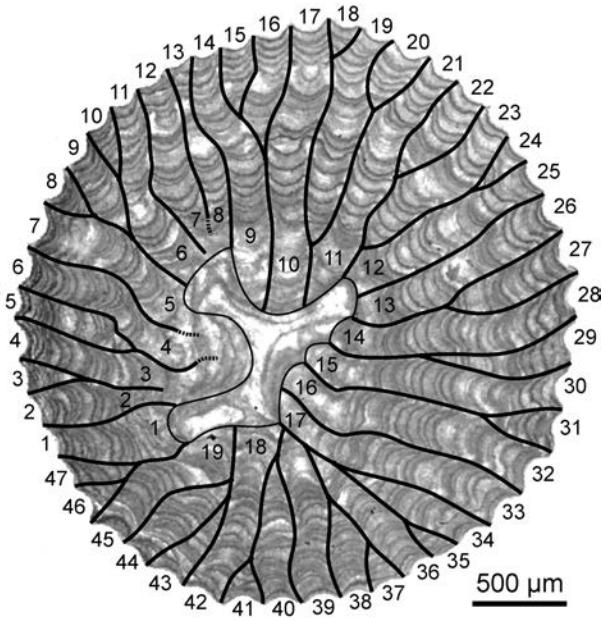

FIGURE 4. OM stained section (same as Fig. 2a) and identification of the columns of crenulations.

Figure 4. This figure shows that the appearance of new columns of wavelets occurs at ridge triple junctions (or nodes). Twenty-eight nodes have been identified but they are not evenly distributed: some ridges are devoid of nodes but others can have three of them, generating two-dimensional tree-like structures. The diameter of the red coral skeleton changes also from the base of the trunk to the tip of the branch, with irregularities at branch junctions. Here again, changes in diameter at the surface of the skeleton are accommodated by a changing number of striations and not by a significant change of their wavelength. Appearance and disappearance of crenulations occur at nodes as shown in Figure 1c [A]. As mentioned earlier, the locations of the polyps correspond to more or less pronounced cavities at the surface of the skeleton, especially along branches with relatively small diameters. In this respect, the stained section shown in Figure 2b is particularly informative since the morphology in the living tissue (Fig. 2b [B]) indicates that the section passes through the location of a polyp. In agreement with the observations at the surface of the skeleton, wavelets are absent at the bottom of the cavity of the polyp (Fig. 2b [B]).

SEM observations in back-scattered mode of polished sections show that the internal structure of a wavelet is chemically complex. Figures 5a and 5b display two examples. Variations in gray levels indicative of compositional variations are observed down to the micrometer scale. At first, chemical heterogeneities seem to be arranged in nicely organized parallel bands of variable thicknesses (Fig. 5a) and six growth rings can be recognized. However, a closer look and observation of another sample (Fig. 5b) indicates that interfaces between bands of different compositions are locally irregular. The complexity of chemical banding is such that the identification and counting of the growth rings is difficult. Lines joining the crests (white dashed lines and diverg-

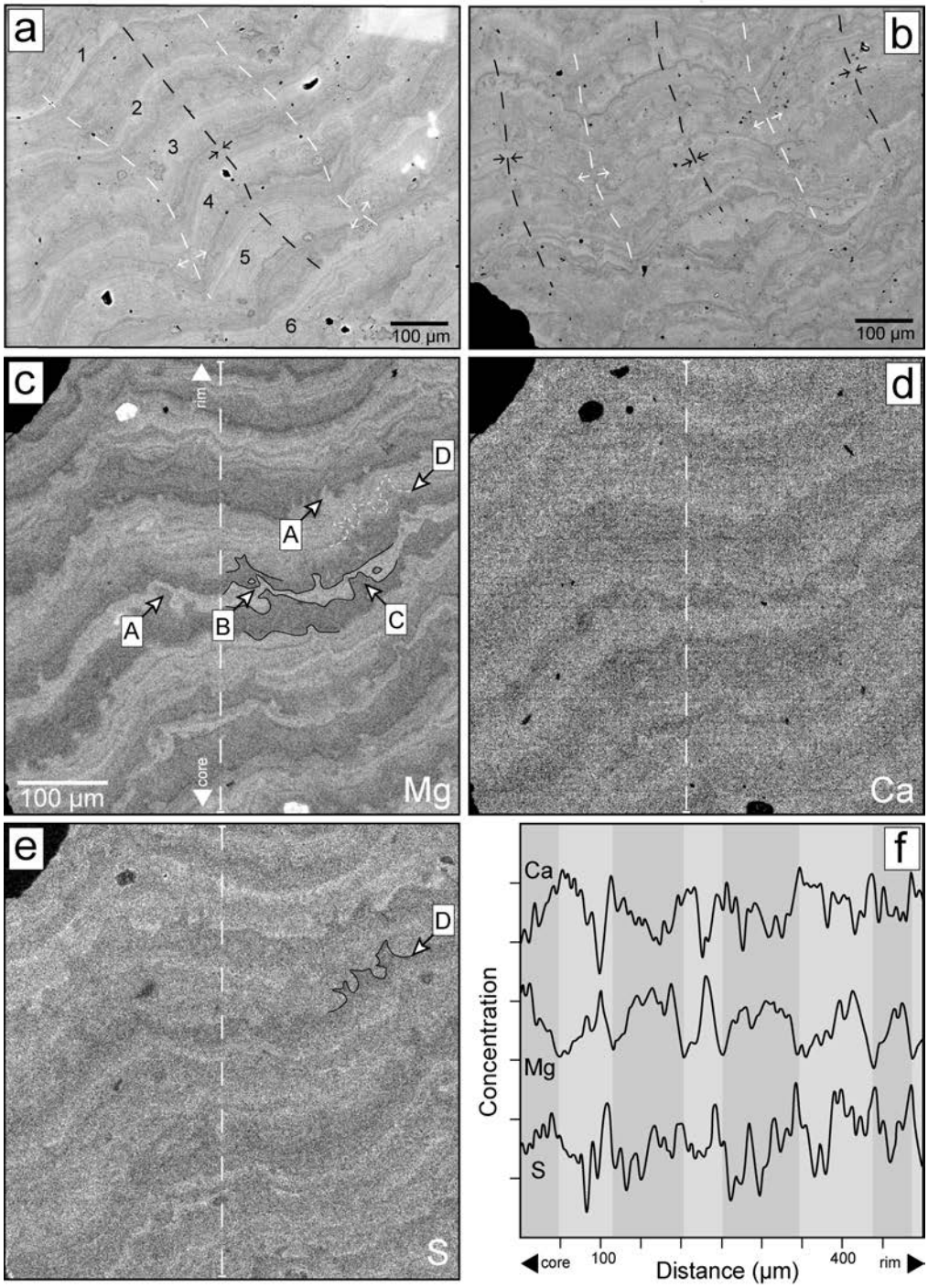

FIGURE 5. SEM back-scattered electron images and electron microprobe X-ray maps of different sections of red coral skeleton at high magnification. (**a** and **b**) SEM back-scattered electron images of two sections: variations in gray levels are indicative of compositional variations. Note the complexity and richness of the signal. Interfaces between bands are locally irregular. Six annual growth rings (marked 1 to 6) are identified in **a**. Lines joining the crests (white dashed lines and diverging arrows) and the troughs (black dashed lines and converging arrows) of the wavelets have been drawn to facilitate the interpretation of the photographs. (**c** to **e**) Electron microprobe X-ray maps of Mg, Ca, and S in a polished section of red coral skeleton at high magnification. (**c**) Magnesium image allowing the identification of seven annual growth rings. The interfaces between Mg bands are tortuous and indicate the presence of microprotuberances. (**d–e**) Calcium and S images (same location as **c**). (**f**) Plot of gray levels obtained by processing the Mg, Ca, and S images along a traverse (shown as a vertical dashed line on **c**, **d**, and **e**). Note the anti-correlation between Mg and Ca and that the most prominent S spikes coincide with low concentrations of Mg. Vertical gray bands mark the seven annual growth rings identified by variations in Mg concentrations.

ing arrows) and the troughs (black dashed lines and converging arrows) of the wavelets have been drawn on Figures 5a and 5b to facilitate the interpretation of the photographs. Crests and troughs show identical chemical features. Figures 5c–5e show X-ray images of Mg, Ca, and S of another sample at relatively high resolution. The Mg image is particularly sharp and allows the identification of seven growth rings. Like on the SEM images, variations in concentrations are observed down to the micrometer scale. The interfaces between bands of different Mg content are tortuous. Microprotuberances responsible for the tortuosity are observed in both Mg-rich and Mg-poor layers (Fig. 5c [A]). The Ca and S images (Figs. 5d and 5e) are not as sharp as the Mg image. This is because the variation in concentration of Ca is low in comparison with the average Ca concentration in the material. On the other hand, the relatively poor quality of the S image comes from the low concentration of this element in the material, generating a low signal/noise ratio. Plots of gray levels obtained by processing the Mg, Ca, and S images along a traverse (shown as a vertical dashed line on Figs. 5c, 5d, and 5e) allow the observation of a clear anti-correlation between Mg and Ca (Fig. 5f). The relations between the concentration of S vs. Ca or Mg are not so clear, but the most prominent S spikes coincide with low concentrations of Mg, and thus, with high concentrations of Ca.

Microprotuberances

The surface of the axial skeleton provides critical observations for deciphering the internal architecture of the skeleton as it represents a "frozen" isochron surface of growth. This surface is entirely covered with microprotuberances, uniformly distributed on the surface (Fig. 6a). These structures display complex arborescent shapes (Figs. 1c and 1e in Grillo et al. 1993 and our Fig. 6a). The density of these microprotuberances at the surface of the skeleton is high: for instance, Grillo et al. (1993) counted an average of ~700 of them per square millimeters. Their height ranges from 0 to ~20 μm and the distance between two adjacent structure axes is about 30 μm. These microprotuberances develop secondary and ternary branches that point outwards most of the time; however, some of the branch tips point inwards and coalesce with the basement layer (Fig. 6a [A]). This observation indicates that the diametric growth of the skeleton is not always centrifugal. In addition, branches from two initially separated microprotuberances can interconnect, form bridges (Fig. 6a [B]), and thus generate a complex three-dimensional network. Microprotuberances seem to be part of, and emerge from a continuous layer made of more or less densely packed calcite crystals (Fig. 6b). Inside the axial skeleton, such layers with characteristic microprotuberances can be recognized (Figs. 6b and 6c). Observations with the SEM of sections that were broken or polished then slightly etched indicate that the axial skeleton corresponds to the stacking of microprotuberance layers (Figs. 6b, 6c, 6e, and 6f). In some cases, the interface between two microprotuberance layers corresponds to a marked physical discontinuity (Figs. 6b and 6c [A]).

An important objective was to determine whether microprotuberance layers correspond to a particular chemical composition (possibly indicative of seasonal growth). In this respect, X-ray maps are informative. Figure 5c shows that microprotuberances are found in all of the chemical layers (e.g., Fig. 5c [A]). In addition, a given microprotuberance can persist in layers of different compositions (e.g., Fig. 5c [B]) or, in contrast, suddenly stop and be buried in the next layer (Fig. 5c [C]). A word of caution is required here, since a microprotuberance is a three-dimensional structure, its disappearance on a two-dimensional image can be simply due to a cross-section effect. Figure 6e indicates that microprotuberances can grow on top of previous ones, and that this piling up can persist over distances ≥100 μm, or in other words, over long periods of time (see below). On electron microprobe X-ray images, microprotuberances are detected because of compositional contrast. Thus, on such images, the number of microprotuberances can be underestimated because some of them could be present in layers of constant composition and remain undetected. This finding is in agreement with the fact that microprotuberances identified on the S image do not always coincide with microprotuberances visible on the Mg image (compare Fig. 5c [D] and Fig. 5e [D]). Microprotuberances are relatively large-scale structures (10–50 μm). When their trunk or branches are broken, an internal substructure can be observed (Figs. 6d and 8a). There, the tiny calcite crystals are organized in concentric rings and may form micrometer-sized pipes or cones.

Fibers, blades, and fan-shaped bundles

As can be observed with the SEM on broken sections of skeleton, the presence of crystalline fibers (Fig. 7d) or blades (Fig. 7c) whether organized or not into superstructures [fans (Fig. 7a) or concentric rings (Fig. 7b)], is a common feature in the red coral. The length of the crystalline blades or fibers ranges from ~1 to ~10 μm, whereas their width is commonly <1 μm. In some cases, the tiny fibers are organized into branch-like structures (Figs. 7d and 7e) and resemble the general shape of the colony. However, crystalline fibers are not observed everywhere in the skeleton with the SEM, possibly as a consequence of cross-section effects, and the detailed structural relationships between microprotuberances, fibers, and fan-shaped structures remain to be clarified.

At this stage, it is important to determine if blades and/or fibers correspond to single crystals of calcite. Observations of etched surfaces at high magnification under the SEM indicate that, in spite of the small size of these structures, blades or fibers do not correspond to single crystalline units but are rather made of the piling up of well-aligned sub-units (Figs. 7f, 7g, 7h, 7i, and 8e).

Submicrometer crystalline units

Figure 8 shows a series of SEM images of submicrometer crystalline units at high magnification. These units display different shapes and sizes: in general, they correspond to platelets or more or less isometric grains. Their size varies from a few tens to a few hundreds of nanometers. The exact range of size is difficult to determine because the largest units can be mistaken for poly-crystalline fibers. In some cases, the change in size from one layer to another is obvious (Figs. 8b and 8d). Some well-marked microprotuberance layers are made of particularly small submicrometer crystalline units (Figs. 8b and 8d).

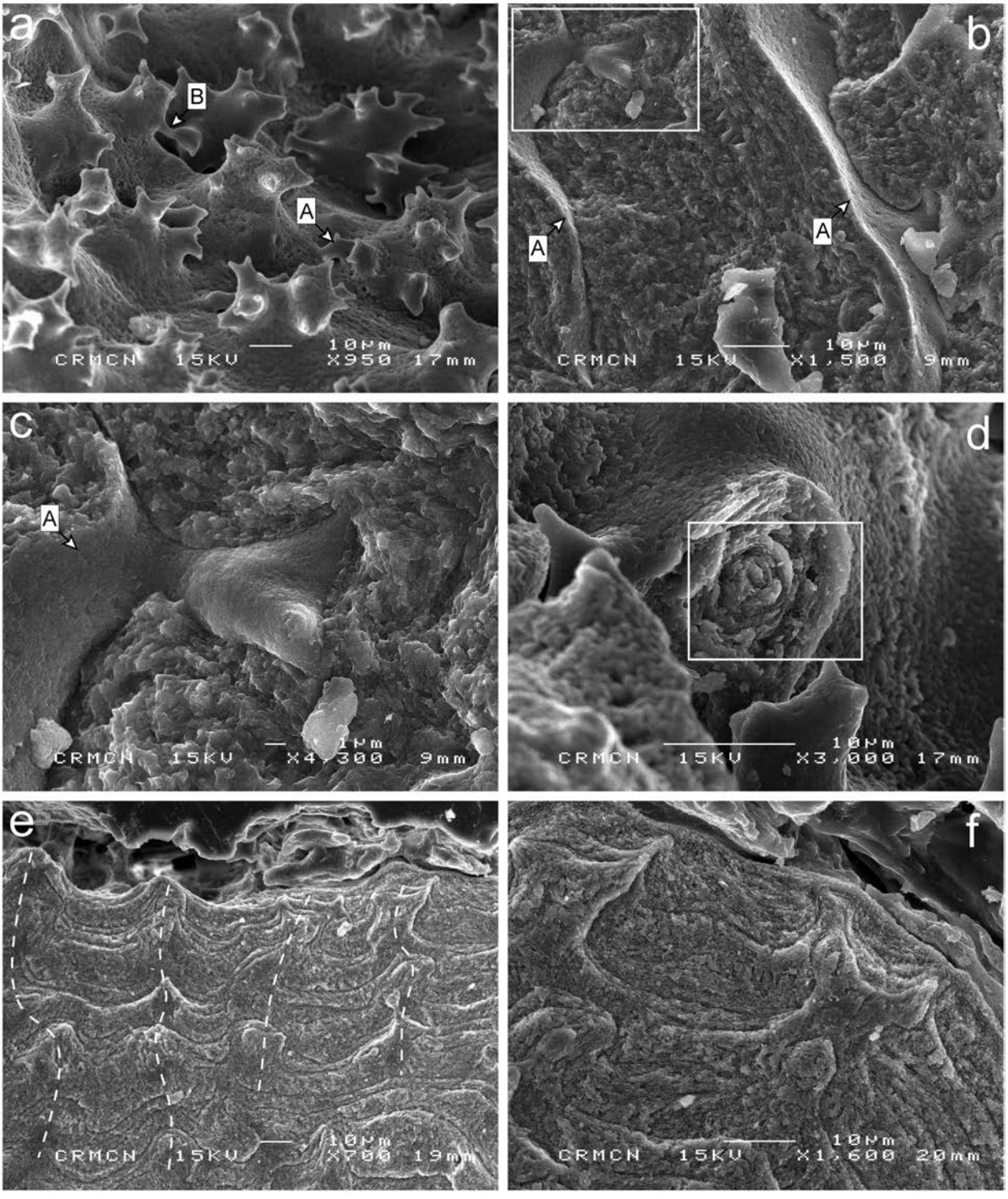

FIGURE 6. SEM images in secondary electron mode of red coral skeleton. (**a**) Surface of the axial skeleton showing microprotuberances. (**b**) Broken section showing the stacking of protuberance layers and discontinuities between layers. (**c**) Enlargement of **b** showing a microprotuberance encased in a crystalline layer. (**d**) Internal structure of a microprotuberance and radial arrangement of crystalline units. (**e**) Stacking of microprotuberance layers on a polished then etched surface of a section of red coral skeleton. The white dashed lines mark the central axis of some microprotuberances. (**f**) Enlargement of **e** showing the variation of thickness of the crystalline layers on and in-between the microprotuberances.

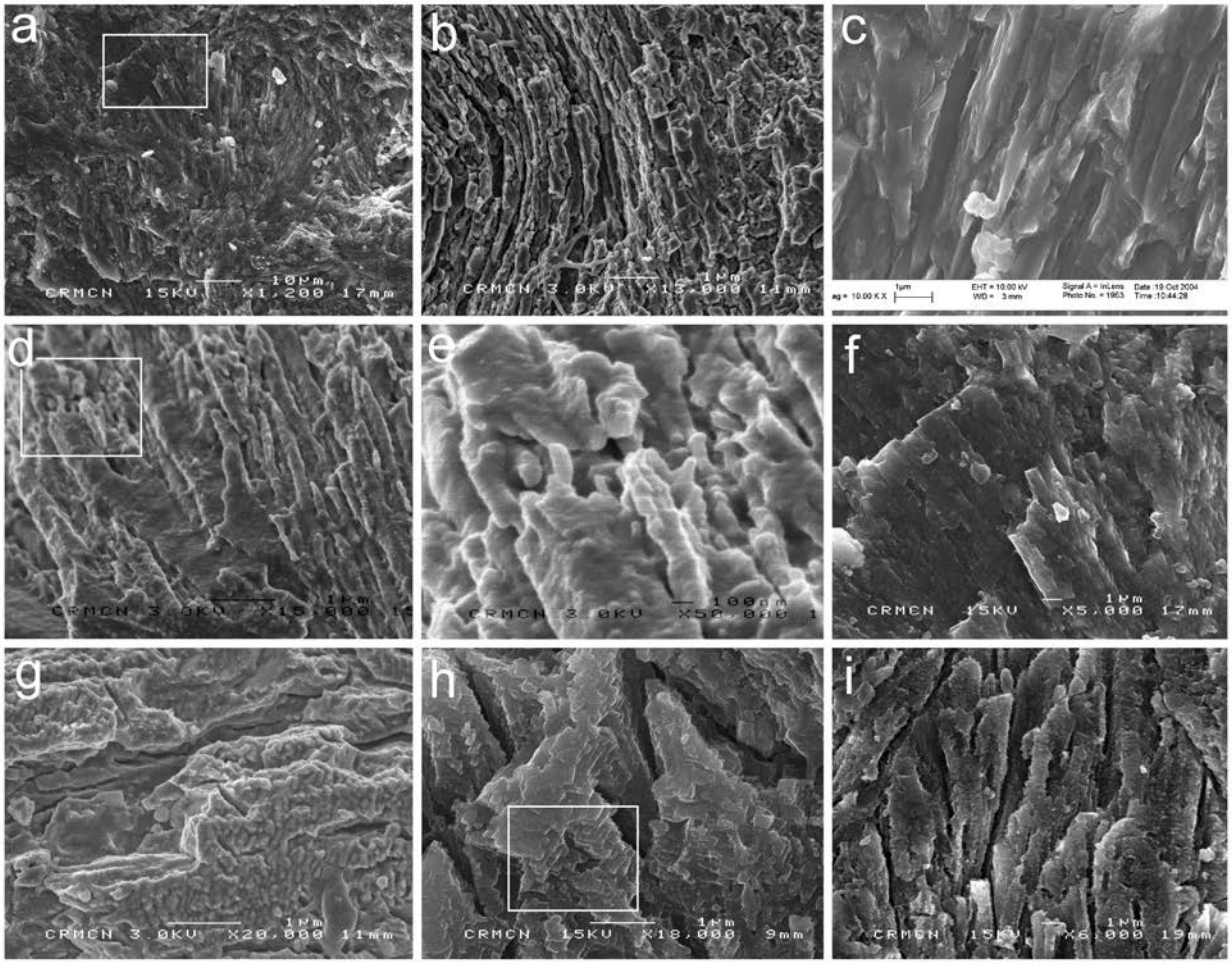

FIGURE 7. Crystalline fibers and blades (SEM in secondary electron mode). (**a**) Arrangement of crystalline fibers in fan-shaped structures (broken section). (**b**) Arrangement of crystalline fibers in circular structures (etched surface). (**c**) Crystalline blades (broken section). (**d**) Crystalline fibers on a etched surface of a section of skeleton. (**e**) Enlargement of **d** showing ramified crystalline fibers. (**f**) Enlargement of **a** crystalline blades at high magnification showing an internal structure. (**g**) Etched surface showing that crystalline blades are made of an aggregation of submicrometer crystalline units. (**h–i**) Polycrystalline fibers and stacking of submicrometer crystalline units (etched surface of a polished section).

To complement the SEM observations, two focused ion beam foils cut perpendicular to each other were prepared from an Mg-poor layer and two others from an Mg-rich layer. TEM observations of these foils (Fig. 9) show the presence of more or less elongated submicrometer crystalline units whose size is commonly around 200–400 nm (Figs. 8f, 9c, 9g, and 9h). Differences in diffraction contrast from one submicrometer crystalline unit to the other can be ascribed to differences in crystallographic orientations. In some cases, the grains are arranged in concentric layers (Figs. 9c and 9h), reminiscent of the internal structure of the microprotuberances (Figs. 6d and 8a) and some arrangements of crystalline fibers (Fig. 7b). Interestingly, an elongated (~10 μm) arborescent unit is observed in Figures 9b and 9d. This latter structure may correspond to the three-dimensional tree-like structures observed to the SEM (Figs. 7d and 7e). In the first FIB section (Figs. 9a and 9b), the crystalline units are rather elongated in contrast with the crystalline units observed in the second, perpendicularly cut, FIB section (Figs. 9e and 9f). In the second FIB foil, the submicrometer crystalline units are often zoned in terms of diffraction contrast with a homogeneous core surrounded by a heterogeneous rim. Electron diffraction patterns (not shown here) collected in different zones in Figure 9b indicate that the submicrometer units diffract as single crystals, which does not mean that the areas of interest are monocrystalline as will be seen later. In the dark-field images (Figs. 9c, 9g, and 9h), grain boundaries are commonly marked by thin (continuous or not) black spaces indicative of porosity. No significant difference was found between FIB foils recovered in layers of different Mg concentrations but further observations are required. Finally, it is interesting to note that the submicrometer structure observed in the main skeleton can also be observed in the sclerites (Fig. 9h).

Some of the features observed on the polished-then-etched surfaces and interpreted as indicative of the presence of submicrometer units (e.g., Fig. 8e), could be due to the recrystallization of calcite caused by dissolution/reprecipitation during etching

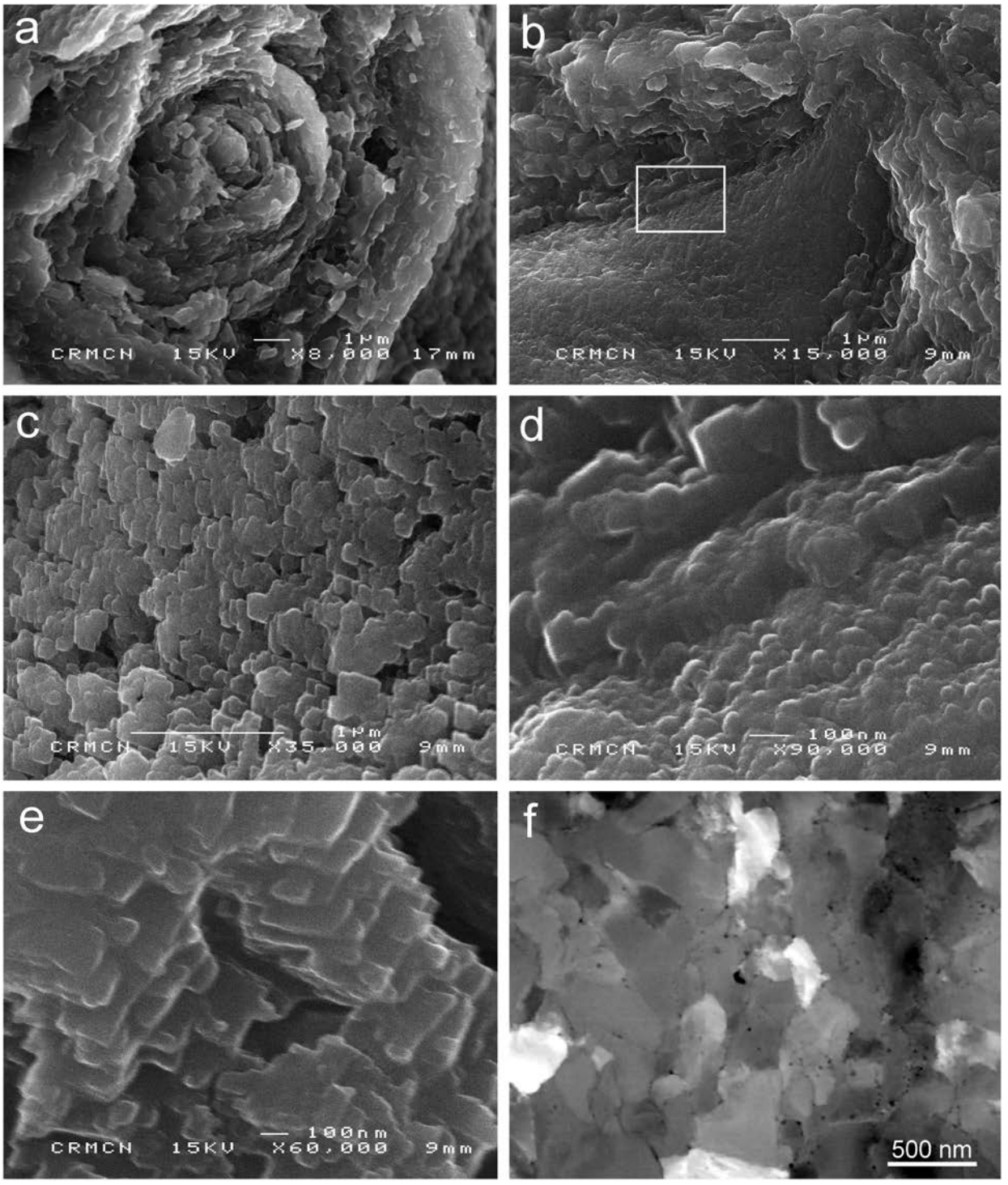

Figure 8. Submicrometer crystalline units (SEM in secondary electron mode and TEM). (**a**) Enlargement of Figure 6d: arrangement of submicrometer crystalline units inside a microprotuberance (broken microprotuberance at the surface of the skeleton). (**b**) Enlargement of Figure 6c: contact between a microprotuberance and the encasing crystalline layer (broken section). (**c**) Platelets of submicrometer crystalline units (broken section). (**d**) Enlargement of **b**. Note the sudden variation of the size of the crystalline units. (**e**) Enlargement of Figure 7h showing the stacking of submicrometer units forming the crystalline fibers. (**f**) TEM observation of a FIB foil of coral skeleton showing the submicrometer crystalline units and rare black areas corresponding to porous space. This picture shows that the porosity is lower than suggested by the SEM images of broken sections or etched surfaces.

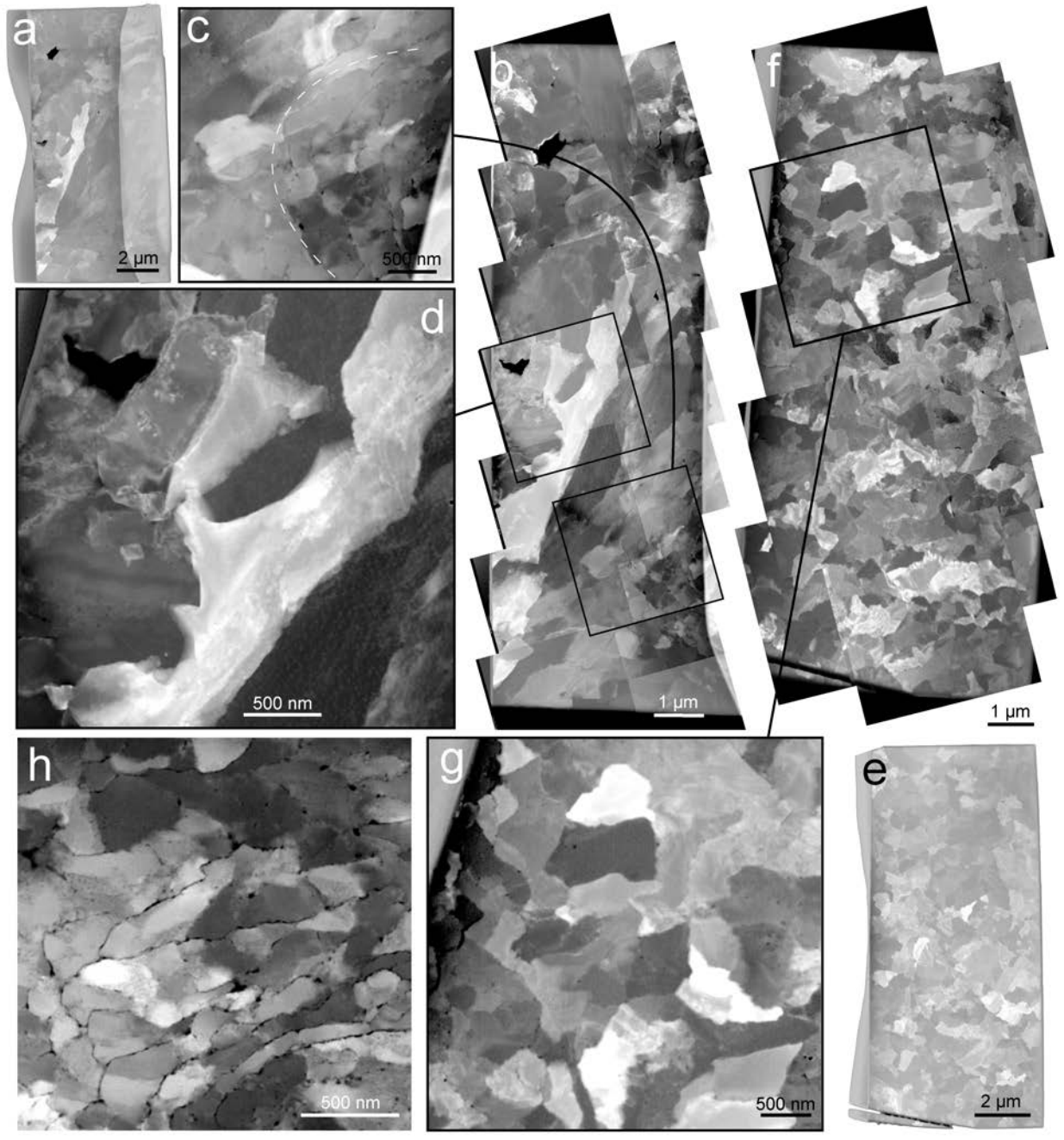

FIGURE 9. TEM observation of FIB foils cut in red coral skeleton (dark-field images). (**a**) General view of FIB foil no. 1. The irregular layer on the left part of the foil corresponds to a protective Pt layer. The lighter gray layer on the right corresponds to a thicker part of the foil. (**b**) Mosaic of images of FIB foil no. 1 showing elongated crystalline domains. (**c**) Enlargement of **b** and concentric arrangement of submicrometer crystalline units underlined by the white dashed line. (**d**) Another enlargement of **b** showing a detail of an elongated crystalline fiber with concave shapes. (**e**) General view of FIB foil no. 2 cut perpendicular to FIB foil no. 1. (**f**) Mosaic of images of FIB foil no. 2 showing that the crystalline fibers are not as elongated as in FIB foil no. 1. Note that the submicrometer crystalline units are zoned in terms of diffraction contrast with a homogeneous core surrounded by a heterogeneous rim. (**g**) Enlargement of **a** showing details of the submicrometer units. Dark spots or thin lines at grain boundaries correspond to porous space. (**h**) Image of FIB foil no. 5 cut in a sclerite. Submicrometer crystalline units are arranged in more or less concentric layers. The black spots or thin lines at grain boundaries correspond to porous space.

and thus may correspond to artifacts. This is a possibility that we do not rule out. However, even in this situation, the fact that calcite recrystallizes with patterns such as those observed in Figure 8e (alignment, size distribution of crystals) can be an indication of the presence of preexisting similarly oriented submicrometer crystalline units. In addition, the fact that submicrometer units are

also observed on untreated broken sections (Fig. 8d), or on FIB foils (Fig. 9h) is clear evidence that they are not artifacts.

Nanodomains

Figure 10a shows a low magnification TEM image of some piano-key like structures that can be interpreted in terms of submicrometer crystalline units. If this interpretation is correct, the units are more elongated than those shown in Figures 9c and 9g. Sets of Bragg fringes (Fig. 9a [A]) define each crystalline unit. The continuity of the fringes inside a unit is an indication of good crystal quality and same crystallographic orientation within each unit. The boundary between two units is marked by a diffuse zone indicative of poorer crystal quality. In such zones, variations in diffraction contrast indicate the presence of nanopores (Fig. 10a [B]), which is consistent with observations in Figures 9g and 9h. Unexpectedly, TEM observations at higher magnification indicate that the submicrometer crystalline units identified on the FIB sections may not be single-domain crystals. Instead, they are made of an assemblage of nanodomains whose size ranges from 2 to 5 nm. Flat and curved nanodomain surfaces can be observed (Fig. 10b [A and B]). Variations in absorption contrast in the image and the presence of free crystalline surfaces suggest the presence of an intimate network of nanopores. High-resolution TEM imaging (Fig. 10c) confirms the previous observation: submicrometer crystalline units are made of 2–5 nm perfect nanodomains of Mg-calcite with neither dislocation nor twin lamellae. Each domain is considered monocrystalline because lattice fringes are observed in the high-resolution images. Low contrast between crystalline (lattice-fringe-bearing) regions together with the observation of crystalline facets suggest that space separates adjacent domains. Most importantly, the parallelism of lattice fringes across adjacent domains demonstrates that the crystallographic axes of all domains are nearly parallel. TEM Images shown in Figures 10a to 10c were obtained on samples thinned by ion-milling. Since some artifacts can be caused by this preparation technique, observations were duplicated using powdered material; they confirmed the presence of nanodomains. In addition, the transformation of calcite into lime (CaO) was observed after long exposure to the beam. Thus, care was taken not to leave the sample under the electron beam for long durations. Thus, although this possibility cannot be entirely ruled out, we anticipate that nanodomains are not artifacts due to radiation damage.

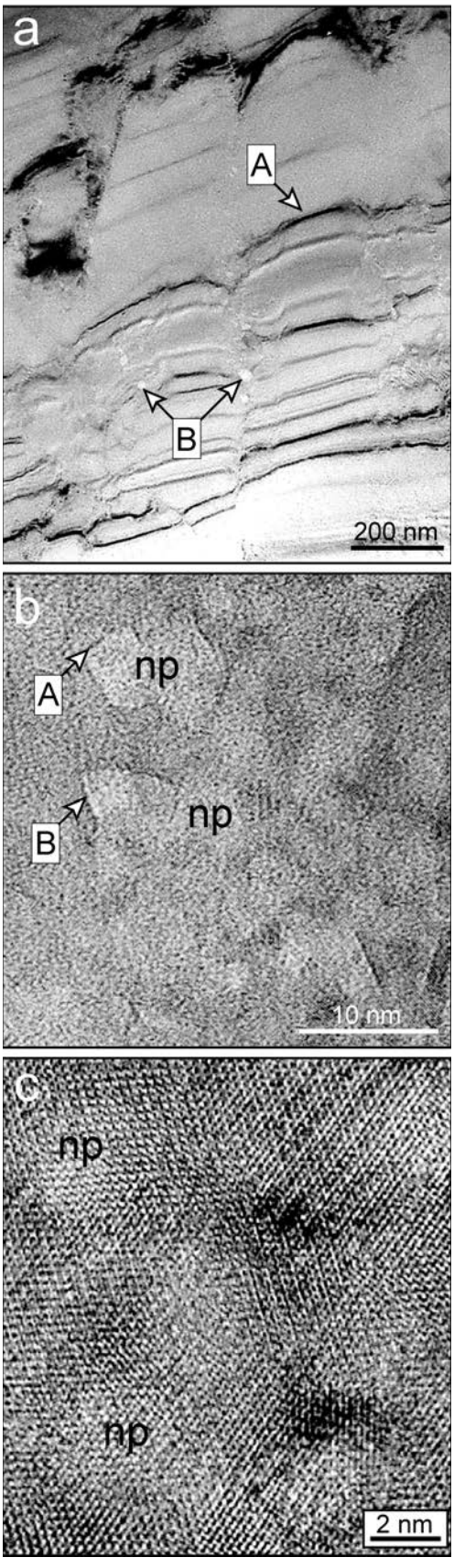

►**FIGURE 10.** TEM images of samples prepared by ion mill. (**a**) Low-magnification TEM image of piano-key like structures. The sets of continuous Bragg fringes [A] define crystalline units. Contrast variations indicate the presence of nanopores [B]. (**b**) TEM image showing that the internal structure of the submicrometer units is made of an assemblage of 2–5 nm nanodomains. Variations in absorption contrast indicate the presence of nanopores (np). (**c**) High-resolution TEM image of lattice fringes of Mg calcite indicating that each nanodomain is monocrystalline. The parallelism of lattice fringes demonstrates that the crystallographic axes of all domains in the area are nearly parallel. Low contrast between crystalline regions indicates the presence of porosity (np) at that nanoscale.

DISCUSSION

In this section, the hierarchical structure of the red coral skeleton will be considered from the nanometer to the centimeter scale, in a bottom-up order.

Nanograins and submicrometer units

The observation of 2–5 nm domains in the submicrometer crystalline units is important since it has implications for the mechanisms of crystal growth in living organisms. The nanodomains and the associated nanoporosity observed in 2D images can be the expression of (1) nanograins or (2) domains belonging to nanoporous crystals with sponge-like morphologies. In the literature, there is increasing evidence that inorganic nanograins made up of thousands of atoms can be building blocks for the construction of biominerals (Alivisatos 2000). In this context, a "mesocrystal,"—synonymous of defective single crystal—is defined as a superstructure made of more or less similarly oriented crystalline particles (see Cölfen and Antonietti 2005 for a review). These new concepts derive from the observation and characterization of both experimental run products (Penn and Banfield 1999) and natural samples (Banfield et al. 2000). An important point is that, in spite of being made of the aggregation of nanoparticles, mesocrystals display scattering behavior of single crystals. Recently, biominerals including bones, nacreous layers of seashells, stereom of sea urchin spines, diatoms, and Fe-oxidizing bacteria have been reported to be constructed of nanoscale building blocks (see Oaki et al. 2006 for a review). However, a word of caution is required here since the term "nano" is used in the literature for sizes ranging from one to several hundreds of nanometers. This fact complicates the intercomparison of biomineral structural units in different organisms. In the present study, "nano" will be used for structural units <10 nm. In the literature, nanograins (<10 nm) rarely have been documented. Such nanograins have been observed in calcite sponge spicules by Sethmann et al. (2006) who reported the presence of more or less well-aligned ~2–5 nm crystal domains (i.e., nanograins, their Fig. 3c) forming ~50–100 nm crystalline superstructures (their "nano-cluster blocks," our "submicrometer units"). Banfield et al. (2000) examined biomineralization products of Fe-oxidizing bacteria and showed that oxy-hydroxide crystals were made of assemblages of 2–3 nm particles. Previously, Penn and Banfield (1999) demonstrated experimentally that long chains of highly ordered TiO_2 could emerge from a solution of nanoparticles, and that primary particles could align, dock, and fuse to form oriented chains by a mechanism of "oriented attachment." This mechanism elaborated on the concept of "particle aggregation" developed in colloids (Bailey et al. 1993; Privman et al. 1999) seems to apply widely in biomineralogy as shown by a series of biomimetic experiments in the $CaCO_3$ system (see Cölfen and Antonietti 2005; Imai et al. 2006 for reviews). These studies emphasized the role of the medium of crystallization (gels) and the presence of organic molecules that may play the role of "assemblers." Organic molecules would be subsequently trapped between the inorganic building blocks, making the end-product a composite material. In the case of calcitic sponge spicules, combined high-resolution and energy-filtering transmission electron microscopy revealed C enrichment located between nanograins, suggesting an intercalated network-like proteinaceous organic matter (Sethmann et al. 2006). The presence of nanoporosity is another salient feature of mesocrystals. Wang et al. (2006) measured specific surface areas of several hundred of m^2/g for synthetic $CaCO_3$ mesocrystals prepared with a polystyrene sulfonate additive. Cölfen and Antonietti (2005) noted that even if the nanoparticle arrangement is almost perfect in mesocrystals, the porosity can be high as a result of grain polydispersity and stacking defects during aggregation. According to these authors, the defects could be transformed into pores with inclusions of organic molecules upon ripening to a single connected crystal. This transformation was observed in the time-dependent experiments carried out by Judat and Kind (2004) on Ba-sulfate mesocrystals. At present, in the red coral skeleton, we favor the interpretation that submicrometer units are mesocrystals made by the aggregation of oriented nanograins preserving some porosity at the interfaces. The pores would be occupied, in part, by organic molecules. In this interpretation, aggregates of particles share the same three-dimensional orientation, which explains the apparent contradiction of having continuous Bragg fringes and monocrystalline SAED patterns (not shown here) in non-monocrystalline submicrometer units. We do not entirely rule out the possibility, and indeed this is the preferred interpretation of one of us (A.B.), that the submicrometer units could be sponge-like crystals, i.e., crystals with a perfect crystallographic continuity, with voids (connected or not) within them. In any case, decisive crystallographic observations in favor of one interpretation or the other remain to be done but will be difficult especially as sponge-like crystals may correspond to a stage following the aggregation of oriented particles and the ripening of the nanograin assemblage into a single connected crystal (Inumaru 2006; Schwahn et al. 2007). In recent years, in biomineralization processes, the interest has been focused more on the role of amorphous $CaCO_3$ (ACC) precursor (Addadi et al. 2006) than on the aggregation of oriented nanoparticles. However, the existence of nanograins does not exclude the presence of ACC precursor. Addadi et al. (2006) noted that there is a logistical problem of transport of ions and removal of water from the mineralization site considering the volume of $CaCO_3$ deposited and the solubility of $CaCO_3$ in the solution. According to these authors, one possibility would be to form precursor subunits elsewhere and transport them to the mineralization site. The presence of nanograins can fit into such a scheme of processing at multiple levels.

If we define a fundamental brick as the largest structural unit omnipresent in the superstructure, the submicrometer unit described earlier is indeed the fundamental brick for the construction of the red coral skeleton, even if the brick itself is made of nanoscale subunits. Atoms or nanograins are other obvious units but are not considered here as fundamental bricks since they do not correspond to the "largest" structural building unit. Note that the choice of the submicrometer unit as the fundamental building block of the red coral skeleton is compatible with both interpretations of the internal structure of the submicrometer units: assemblage of nanograins or sponge-like crystals. As discussed earlier, submicrometer units display a range of sizes from a few tens to a few hundreds of nanometers. Such building blocks are commonly observed in biominerals: calcitic sponge spicules (~50–100 nm, Sethmann et al. 2006); mollusk nacre

(~45 nm, Dauphin 2001; Rousseau et al. 2005; Oaki et al. 2006); skeletal element of the sea urchin (~30–50, Sethmann et al. 2005; Oaki et al. 2006); coral (~100 nm, Oaki et al. 2006); foraminifer (~10–20 nm, Oaki et al. 2006); eggshell (~20–30 nm, Oaki et al. 2006). Thus, submicrometer crystalline units seem to be a feature that many (if not all) biomineral structures have in common. Obviously, considering the range of sizes of these building blocks, some uncertainty may persist upon classifying them as submicrometer units or nanograins. Only detailed HRTEM study on each of these organisms may indicate whether these units are already superstructures or not.

Fibers, blades, and fans

SEM observations indicate that etched fibers and blades ranging in size from a few micrometers to a few tens of micrometers are made of an assemblage of submicrometer units (Figs. 7f and 8e). This finding is in agreement with the phase image-AFM obtained by Dauphin (2006) indicating that each fiber in red coral is composed of rows of ~100 nm granules. The alignment of individual submicrometer units and parallel shapes of units suggest similarities in crystallographic orientations between crystallites. This interpretation is in agreement with the observation of elongated crystalline fiber in the FIB foil shown in Figure 9b that may correspond to the piling up of submicrometer units with similar crystallographic orientation. If this interpretation is correct, part of the structural anisotropy observed in the skeleton structure—for instance, by a comparison of two perpendicular FIB foils (Figs. 9b and 9f)—could be ascribed not to the size of the submicrometer crystalline units but to their organization in elongated crystalline fibers. Thus, fibers and blades, or at least some of them, could be seen as mesocrystals of second order (while the submicrometer unit would be a mesocrystal of first order). Again, the distinction between submicrometer unit and fiber can be ambiguous because of a possible overlap of sizes; for instance the piano-key like structures shown in Figure 10a interpreted earlier as submicrometer units could be also interpreted as fibers made of the piling up of submicrometer units with similar crystallographic orientations.

Micrometer- to tens of micrometer-sized $CaCO_3$ mesocrystals are classically observed in experiments carried out in presence of organic molecules (Niederberger and Cölfen 2006; Imai et al. 2006). In 1986, Dominguez-Bella and Garcia-Ruiz carried out $CaCO_3$ crystallization experiments in silica gel. They reported the presence of micrometer-sized fibers made of calcite rhombohedra aligned along their **c**-axes. Though each fiber corresponded to an aggregate of crystalline subunits, observation under cross-polarized light indicated single-crystal behavior resulting from the high orientational alignment of the subunits

Layers and microprotuberances

Submicrometer units, fibers, and blades are different substructures used to build layers. The thickness of the layers varies both from one layer to another and along the same layer, depending on the position between (thick) or on top (thin) of the microprotuberances (Figs. 6e and 6f). Because of resemblance between sclerites and microprotuberances, Lacaze-Duthiers (1864) suggested that the formation of the axial skeleton resulted from the migration of the sclerites from the mesoglea and aggregation in a calcareous cement at the surface of the skeleton. This is a critical hypothesis since the taxonomy of *Corallium* is based on this criterium (Allemand 1993). Allemand and Bénazet-Tambutté (1996) confirmed that sclerites could be directly incorporated in the apical part of the coral colonies to form the medullar zone of the axial skeleton. However, concerning the annular part of the skeleton, Grillo et al. (1993) and Allemand and Bénazet-Tambutté (1996) rejected the Lacaze-Duthiers interpretation. They showed that microprotuberances are smaller, more spinose, and less numerous per surface unit than sclerites. In addition, biocalcification kinetic experiments using ^{45}Ca as a tracer indicated that there was no delay in the calcification of sclerites and annular skeleton as would be expected if the skeleton was made of sclerite aggregation (Allemand and Grillo 1992). The absence of calcareous cement, the presence of calcitic microlayers much thinner than a single sclerite, the observation of deeply rooted microprotuberances, and the continuity of the layer in and out of the microprotuberance are in disagreement with the interpretation proposed by Lacaze-Duthiers for the formation of the annular part of the skeleton. Interestingly, the work of Grillo et al. (1993) showed that (1) the cellular structure secreting a sclerite in the mesoglea (scleroblast) is identical to the axis epithelium (surrounding the axial skeleton) with respect to the cellular organization and structure; and (2) that patterns of growth and mineralogy of the axial skeleton and sclerites are fundamentally identical. Thus, scleroblasts on one side and axial epithelium on the other side would secrete new layers of calcite on sclerites or axial skeleton by an identical process but at two different locations.

If the spicules are not bricks for the construction of the annular part of the axial skeleton, what is their function and what is their fate? Kingsley (1984) proposed several functions for sclerites: sensory receptor, stability device, protection against predator, and mechanical protection against abrasion. Allemand (1993) suggested that the main function of sclerites was to ensure mechanical protection against abrasion, a function consistent with the high rate of sclerite synthesis and renewal in red coral. According to that author, this hypothesis is further supported by the observation of free (expelled?) sclerites at the base or near the colonies. We anticipate another function for the sclerites: temporary stocks of $CaCO_3$, available upon request for the formation of the axial skeleton by dissolution, transport, and recrystallization mechanisms. This function would solve in part the logistical problem of ion/solution exchange discussed earlier and would imply multiple levels of processing, as commonly observed in biomineralization structures (Mann 2001).

SEM images show the presence of major discontinuities and voids at the interfaces between layers (Fig. 6b). Observations with a petrographic microscope indicate that these planar voids are occupied by OM (Fig. 2). We interpret these discontinuities as markers of interruption of the mineralizing process. If this interpretation is correct, this situation complicates the inversion of the chemical signal (e.g., Mg) registered in the annular rings into external forcing parameters.

Growth rings

The time periodicity of the growth rings marked by Mg is an important question that can be addressed by a comparison with

OM. For chronological purposes, the OM staining method has been calibrated by Marschal et al. (2004) using (1) adult colonies of known age (20 to 22 years); and (2) in situ labeling of colonies with calcein and sampling of the colony one year after. Both calibrations demonstrated the annual periodicity of the OM growth rings. Furthermore, Marschal et al. (2004) determined that the OM-rich parts within annual growth rings developed during winter. Since Mg and OM display the same periodicity and are anti-correlated (Figs. 3a–3d), Mg growth rings are annual and the Mg-rich parts within annual growth rings develop during the hot season. Thus, both oscillations in concentration of OM and Mg/Ca ratio are efficient ways to determine the age of the red coral colonies. More surprisingly, growth features can be used to evaluate the duration of certain physiological events. For instance, growth-ring patterns can be used to determine the lifetime of a polyp in the colony. Indeed, as already mentioned, growth-ring wavelets are absent at the bottom of the cavity of a living polyp. Thus, the absence of crenulation along a growth ring inside the coral skeleton can be interpreted as a mark of a past location of a polyp. On the stained section shown in Figure 2b, two non-crenulated domains corresponding to fossilized locations of polyps can be localized inside the structure (Fig. 2b [C]). These are interstratified between crenulated domains. The counting of the non-crenulated layers in these particular areas indicates that a polyp appears, fulfills its function, and then disappears after 6–8 years of activity. Obviously, complementary observations are required to confirm this hypothesis. Nevertheless, fossilized biomineral structures can indirectly contribute to the understanding of the biology of an organism.

Magnesium mapping is a new, fast, non-destructive method to date red coral colonies. It is an efficient method even in the oldest parts of the colonies. It confirms the conclusions obtained by the OM-staining method that the growth rate of red coral is slower than previously thought and that two-dimensional images are better than profiles to identify and count the growth rings. This is due to the fact that (1) the intensity and width of growth rings can vary laterally and (2) a growth ring is made of the piling up of the complex shaped and interlocked layers. As a consequence, a profile along a radius of an axial skeleton will not translate everywhere into a monotonic temporal evolution. In this study, a spatial distribution of Mg oscillations is observed on several colonies with a wavelength significantly smaller than the one depicted by Weinbauer et al. (2000). This is probably due to the fact that the analytical spacing used by these authors was too large to detect 150 μm wavelength oscillations. Since we demonstrated here that Mg oscillations are annual, Mg has a strong potential as an ecological indicator as already proposed by Weinbauer et al. (2000). However, variations in growth rate, suggested by changes in size and shape of crystalline structures, and the presence of frequent hiatuses within the concentric layers may complicate the determination of relations between composition and external forcings.

Concluding remarks

The red coral skeleton is an example of complex material that exhibits hierarchical structural order on length scales from nano- to macroscale. It is not yet clear whether this structural hierarchy is a direct product of biocrystallization or the result of early diagenesis, as suggested by one of the reviewers. However, we favor the first interpretation because structures observed at the surface of the skeleton are also found inside it (e.g., microprotuberances). Porosity observed at all scales combined with 2D mapping of OM indicates that the red coral skeleton is also a composite organic/inorganic material. The presence of OM at all scales suggests organic control over crystallization, growth, and hierarchical organization of the skeleton. A chemical multiscale and oscillatory structure is superposed upon the physical organization. It provides a means to date colonies of coral and brings constraints for deciphering biomineralization processes. Self-similarly patterns appeared twice. For instance, two levels of mesocrystals have been identified: the submicrometer unit is possibly a superstructure assembled by a three-dimensional oriented aggregation of calcite nanoparticles, whereas crystalline fibers are superstructures assembled by a three-dimensional oriented aggregation of submicrometer units. In addition, three levels of arborescent structures have been identified: arborescent crystalline fibers, bush-like microprotuberances, and tree-like colony itself. The implications in terms of growth mechanisms remain to be explored. Red coral is, among others, a clear example of bottom-up fabrication of a complex superstructure from nano- to micro-scale, multiple-sized structural units.

Acknowledgments

This work has been supported by Centre National de la Recherche Scientifique—Institut National des Sciences de l'Univers (INSU) through grant ECLIPSE 2005 and by Centre Interdisciplinaire de Nanosciences de Marseille through internal grants to D.V. We thank C. Henry for his support. We thank J.-L. Devidal, Ma Chi, and E. Reusser for their assistance with electron microprobes and SEMs, and C. Vanni, W. Saikali, C. Dominici, and T. Neisius for their help with the FIB foil preparation and observation at CP2M. We made the TEM observations in the INSU TEM facility at Marseille. We thank S. Nitsche and D. Chaudanson for their supervision during the TEM sessions. This paper benefited from several constructive discussions with F. Bonneté, N. Floquet, D. Chatain, D. Allemand, and S. Bénazet-Tambutté. Reviews by two anonymous reviewers as well as editorial handling by Pupa Gilbert are gratefully acknowledged.

References cited

Addadi, L., Joester, D., Nudelman, F., and Weiner, S. (2006) Mollusk shell formation: A source of new concepts for understanding biomineralization processes. Chemistry—a European Journal, 12, 981–987.

Alivisatos, A.P. (2000) Biomineralization—Naturally aligned nanocrystals. Science, 289, 736–737.

Allemand, D. (1993) The biology and skeletogenesis of the Mediterranean red coral. A review. Precious Corals and Octocoral Research, 2, 19–39.

Allemand, D. and Bénazet-Tambutté, S. (1996) Dynamics of calcification in the Mediterranean red coral, *Corallium rubrum* (Linnaeus) (Cnidaria, Octocorallia). Journal of Experimental Zoology, 276, 270–278.

Allemand, D. and Grillo, M.C. (1992) Biocalcification mechanism in gorgonians—Ca^{45} uptake and deposition by the Mediterranean red coral *Corallium rubrum*. Journal of Experimental Zoology, 262, 237–246.

Allemand, D., Cuif, J.P., Watabe, N., Oishi, M., and Kawaguchi, T. (1994) The organic matrix of skeletal structures of the Mediterranean red coral, *Corallium rubrum*. Bulletin de l'Institut Océanographique de Monaco, 14, 129–139.

Bailey, J.K., Brinker, C.J., and Mecartney, M.L. (1993) Growth mechanisms of iron-oxide particles of differing morphologies from the forced hydrolysis of ferric-chloride solutions. Journal of Colloid and Interface Science, 157, 1–13.

Banfield, J.F., Welch, S.A., Zhang, H.Z., Ebert, T.T., and Penn, R.L. (2000) Aggregation-based crystal growth and microstructure development in natural iron oxyhydroxide biomineralization products. Science, 289, 751–754.

Barletta, G., Marchetti, R., and Vighi, M. (1968) Ricerche sul corallo rosso, Part IV: Ulteriori osservazioni sulla distribuzione de corallo rosso nel Tirreno. Istituto Lombardo RCB, 102, 119–144.

Cölfen, H. and Antonietti, M. (2005) Mesocrystals: Inorganic superstructures made by highly parallel crystallization and controlled alignment. Angewandte Chemie-International Edition, 44, 5576–5591.

Dauphin, Y. (2001) Nanostructures de la nacre des tests de céphalopodes actuels. Paleontologische Zeitschrift, 75, 113–122.

——— (2006) Mineralizing matrices in the skeletal axes of two *Corallium* species (Alcyonacea). Comparative Biochemistry and Physiology a: Molecular and Integrative Physiology, 145, 54–64.

Dauphin, Y. and Cuif, J.P. (1999) Relationship between mineralogy and microstructural patterns of calcareous biominerals and their sulfur contents. Annales des Sciences Naturelles-Zoologie et Biologie Animale, 20, 73–85.

Dominguez-Bella, S. and Garcia-Ruiz, J.M. (1986) Textures in induced morphology crystal aggregates of $CaCO_3$—sheaf of wheat morphologies. Journal of Crystal Growth, 79, 236–240.

Garrabou, J. and Harmelin, J.G. (2002) A 20-year study on life-history traits of a harvested long-lived temperate coral in the NW Mediterranean: Insights into conservation and management needs. Journal of Animal Ecology, 71, 966–978.

Grillo, M.C., Goldberg, W.M., and Allemand, D. (1993) Sleleton and sclerite formation in the precious red coral *Corallium rubrum*. Marine Biology, 117, 119–128.

Imai, H., Oaki, Y., and Kotachi, A. (2006) A biomimetic approach for hierarchically structured inorganic crystals through self-organization. Bulletin of the Chemical Society of Japan, 79, 1834–1851.

Inumaru, K. (2006) Sponge crystal: A novel class of microporous single crystals formed by self-assembly of polyoxometalate $(NH_4)_3PW_{12}O_{40}$ nanocrystallites. Catalysis Surveys from Asia, 10, 151–160.

Judat, B. and Kind, M. (2004) Morphology and internal structure of barium sulfate—Derivation of a new growth mechanism. Journal of Colloid and Interface Science, 269, 341–353.

Kingsley, R.J. (1984) Spicule formation in the invertebrates with special reference to the gorgonian Leptogorgia-virgulata. American Zoologist, 24, 883–891.

Laborel, J. and Vacelet, J. (1961) Répartition bionomique du *Corallium rubrum* LMCK dans les grottes et falaises sous marines. Rapport Commission Internationale Mer Méditerranée, 16, p. 464–469.

Lacaze-Duthiers, H. (1864) Histoire Naturelle du Corail, 371 p. J.B. Baillière et Fils, Paris.

Liverino, B. (1989) Red Coral, Jewel of the Sea. Analisi, Bologna.

Mann, S. (2001) Biomineralization: Principles and concepts in bioinorganic materials chemistry. Oxford University Press, New York.

Marschal, C., Garrabou, J., Harmelin, J.G., and Pichon, M. (2004) A new method for measuring growth and age in the precious red coral *Corallium rubrum* (L). Coral Reefs, 23, 423–432.

Maté, P., Revenge, S., and Masso, C. (1986) Estudio preliminar de la composicion quimica del coral rojo (*Corallium rubrum* L.) de distintas zonas del Mediterraneo Espanol. Boletin Instituto Espanol de Oceanografia, 3, 53–60.

Mateu, G., Traveria, A., Fontarnau, R., and Masso, C. (1986) Biodiagénesis mineralogica del *Corallium rubrum* (L). Boletin Instituto Espanol de Oceanografia, 4, 1–12.

Meldrum, F.C. (2003) Calcium carbonate in biomineralisation and biomimetic chemistry. International Materials Reviews, 48, 187–224.

Milliman, J.D. (1974) Marine carbonates. Springer, Berlin.

Niederberger, M. and Cölfen, H. (2006) Oriented attachment and mesocrystals: Non-classical crystallization mechanisms based on nanoparticle assembly. Physical Chemistry Chemical Physics, 8, 3271–3287.

Oaki, Y., Kotachi, A., Miura, T., and Imai, H. (2006) Bridged nanocrystals in biominerals and their biomimetics: Classical yet modern crystal growth on the nanoscale. Advanced Functional Materials, 16, 1633–1639.

Penn, R.L. and Banfield, J.F. (1999) Morphology development and crystal growth in nanocrystalline aggregates under hydrothermal conditions: Insights from titania. Geochimica et Cosmochimica Acta, 63, 1549–1557.

Privman, V., Goia, D.V., Park, J., and Matijevic, E. (1999) Mechanism of formation of monodispersed colloids by aggregation of nanosize precursors. Journal of Colloid and Interface Science, 213, 36–45.

Ros, J.D., Gili, J.M., and Olivella, I. (1984) Els sistemes naturals de les Illes Medes. Arxius de la Seccio de Ciencies LXXIII. Institut d'Estudis Catalans, Barcelona.

Rousseau, M., Lopez, E., Stempfle, P., Brendle, M., Franke, L., Guette, A., Naslain, R., and Bourrat, X. (2005) Multiscale structure of sheet nacre. Biomaterials, 26, 6254–6262.

Schwahn, D., Ma, Y.R., and Cölfen, H. (2007) Mesocrystal to single crystal transformation of D,L-alanine evidenced by small angle neutron scattering. Journal of Physical Chemistry C, 111, 3224–3227.

Sethmann, I., Putnis, A., Grassmann, O., and Lobmann, P. (2005) Observation of nano-clustered calcite growth via a transient phase mediated by organic polyanions: A close match for biomineralization. American Mineralogist, 90, 1213–1217.

Sethmann, I., Hinrichs, R., Worheide, G., and Putnis, A. (2006) Nano-cluster composite structure of calcitic sponge spicules—A case study of basic characteristics of biominerals. Journal of Inorganic Biochemistry, 100, 88–96.

Vielzeuf, D., Baronnet, A., Perchuk, A.L., Laporte, D., and Baker, M.B. (2007) Calcium diffusivity in alumino-silicate garnets: an experimental and ATEM study. Contributions to Mineralogy and Petrology, 154, 153–170.

Wang, T., Antonietti, M., and Cölfen, H. (2006) Calcite mesocrystals: "Morphing" crystals by a polyelectrolyte. Chemistry—A European Journal, 12, 5722–5730.

Weinbauer, M.G., Brandstatter, F., and Velimirov, B. (2000) On the potential use of magnesium and strontium concentrations as ecological indicators in the calcite skeleton of the red coral (*Corallium rubrum*). Marine Biology, 137, 801–809.

Manuscript received January 4, 2008
Manuscript accepted May 11, 2008
Manuscript handled by Pupa Gilbert